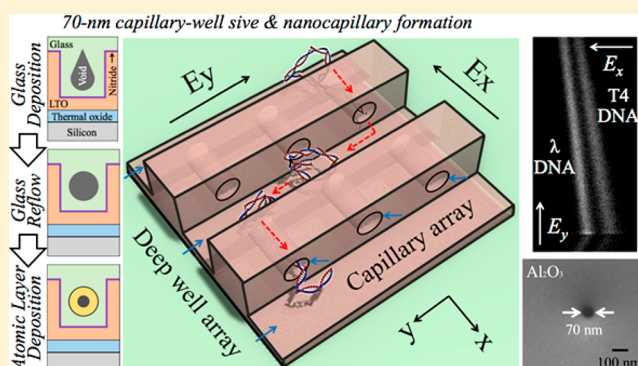


Continuous-Flow Electrophoresis of DNA and Proteins in a Two-Dimensional Capillary-Well Sieve

Lian Duan,[†] Zhen Cao,[†] and Levent Yobas^{*,†,‡,§}[†]Department of Electronic and Computer Engineering, and [‡]Division of Biomedical Engineering, The Hong Kong University of Science and Technology, Clear Water Bay, Hong Kong SAR, China

Supporting Information

ABSTRACT: Continuous-flow electrophoresis of macromolecules is demonstrated using an integrated capillary-well sieve arranged into a two-dimensional anisotropic array on silicon. The periodic array features thousands of entropic barriers, each resulting from an abrupt interface between a 2 μm deep well (channel) and a 70 nm capillary. These entropic barriers owing to two-dimensional confinement within the capillaries are vastly steep in relation to those arising from slits featuring one-dimensional confinement. Thus, the sieving mechanisms can sustain relatively large electric field strengths over a relatively small array area. The sieve rapidly sorts anionic macromolecules, including DNA chains and proteins in native or denatured states, into distinct trajectories according to size or charge under electric field vectors orthogonally applied. The baseline separation is achieved in less than 1 min within a horizontal migration length of ~ 1.5 mm. The capillaries are self-enclosed conduits in cylindrical profile featuring a uniform diameter and realized through an approach that avoids advanced patterning techniques. The approach exploits a thermal reflow of a layer of doped glass for shape transformation into cylindrical capillaries and for controllably shrinking the capillary diameter. Lastly, atomic layer deposition of alumina is introduced for the first time to fine-tune the capillary diameter as well as to neutralize the surface charge, thereby suppressing undesired electroosmotic flows.



Methods that can effectively separate and purify biological macromolecules including nucleic acids and proteins—an important class of biomarkers for the diagnosis of critical diseases—from a complex mixture not only accelerate discovery but also could yield powerful diagnostic tools.^{1,2} Traditional methods typically involve electrophoresis, which acts on the innate electric charge of species and works based on their differential size-dependent electromigration.³ Electrophoresis has brought significant advances despite the limitations often associated with the sieving medium that is required to render the method viable. Gelatinous materials (gels) offer a cross-linked network of pores and are conveniently utilized as the sieving medium. Yet, for sieving relatively large macromolecules (e.g., genomic DNA), gels turn out to be ineffective.^{4,5} Moreover, the random nature of pores in gels increases the complexity of sieving interactions with the migrating macromolecules, and probably, a limited subset of those interactions favors effective separation.⁶ More importantly, such viscous polymeric materials present difficulties for the integration of bioanalytical microsystems.

Artificial sieves refer to micro/nanostructures that present a regular pattern of pores and have been investigated in recent decades for the electrophoresis of macromolecules at an enhanced performance.^{7–10} These structures are shown to outperform gels in separation speed as well as resolution. Further, they are amenable to integration into bioanalytical

microsystems because of their compatible fabrication. Techniques like optical or electron-beam lithography and dry/wet etch are applied on the substrates like silicon or quartz/glass to pattern sieving structures either directly or indirectly through their negative relief template for the subsequent replica molding.¹¹ In many of the sieves, bonding a cover plate is a crucial step to enclose channels and form pores at the interface. However, sieves also exist where the pore formation is independent of the bonding step and realized through alternative means such as the removal of a sacrificial film between layers¹² or the deposition of a structural layer yielding self-enclosed channels.¹³

A host of structures, including post arrays,⁷ asymmetrically placed obstacles,¹⁴ nanowires,¹⁵ self-assembled colloidal arrays,¹⁶ and arrays of alternating slits and wells, the so-called slit-well (SW) motif,⁸ have been reported for sieving macromolecules using the principle of diffusion,¹⁷ asymmetric bifurcation of laminar flow,¹⁸ and entropic trapping.¹⁹ These sieves have been mostly shown to analyze small fractions of mixtures (batch operation) containing large DNA molecules under a constant electric field. Alternating the field in different

Received: June 27, 2017

Accepted: August 16, 2017

Published: August 16, 2017

directions has facilitated fractionation through a hexagonal post array,²⁰ which has later been adopted for a continuous-flow operation.²¹ Continuous-flow fractionation has also been demonstrated with an entropic trap array based on the SW motif.²² In this sieve, the critical pore (slit) dimension can be made comparable to molecular dimensions for the size-based fractionation of small macromolecules such as proteins as well as large DNA molecules.

We have recently demonstrated an entropic trap array where traps arise from two-dimensional (2D) confinement inside capillaries as opposed to one-dimensional (1D) confinement in slits.^{23,24} Macromolecules thus have to overcome relatively steep entropic barriers to migrate through this topography, the capillary-well (CW) motif. This causes a dramatic increase in threshold voltage for the band launching as well as in the voltage range before the sieving mechanism breaks down. Under such high voltage levels, distinct mixtures of proteins and DNA are rapidly resolved into sharp peaks. However, the sieve works only in batch operation, which limits the amount of sample that can be analyzed at a time.

Here, we further extend this structure into a 2D array and demonstrate a continuous-flow fractionation of macromolecules. Figure 1a illustrates a small segment of the array featuring

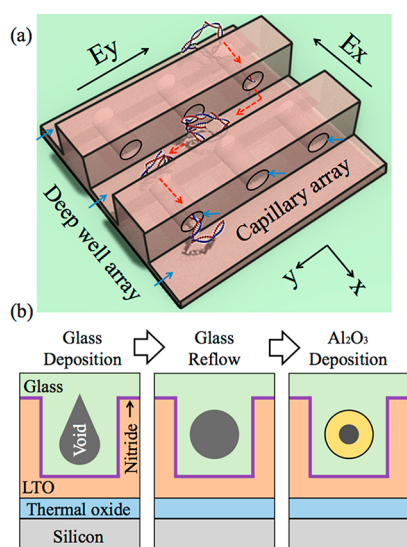


Figure 1. (a) Three-dimensional rendering of an integrated sieve segment with anionic macromolecules being sieved under the influence of orthogonal electric fields E_x and E_y being concurrently applied. (b) Illustrations of a single capillary cross section describing major steps of the integration process.

parallel deep channels (wells) aligned orthogonally to self-enclosed capillaries of a cylindrical profile. Anionic macromolecules being injected into the array through one of the deep channels drift under an average electric field strength applied along the channels, E_y . Concomitantly, drifting macromolecules are selectively driven to jump across the capillaries under an average electric field strength applied along the x -axis direction, E_x . Selectivity depends on the jump dynamics of molecules over the entropic barriers, which is dictated by the steric and electrostatic interactions between the molecules and the sieve walls as previously described.^{19,25,26}

The sieve structure is fabricated as per the integration process of the 1D CW motif previously reported but with a further refinement in the method of defining the capillaries

(Figure 1b). The capillary integration primarily involves (1) patterning trenches within a thick dielectric layer through contact photolithography, (2) depositing a doped glass layer and forming self-enclosed trenches through the shadowing effect of the trench edges, and (3) subsequent thermal annealing (reflow) and shape transformation into cylindrical capillaries.^{27,28} More importantly, thermal reflow is applied for an extended period of time to uniformly shrink the capillary diameter into scales that are accessible typically via advanced patterning tools. Distinct from the process of the 1D CW array, thermal reflow is followed by the atomic layer deposition (ALD) of alumina as the final step for those sieves where the fractionation is through steric interactions. Alumina coating helps quench the surface charge at the operating pH and thus minimize the electroosmotic flows. The continuous-flow fractionation of proteins and DNA in the CW sieve, in relation to the SW design, is realized through a low-resolution array at a reduced pitch length (coarse patterning) and under a high separation voltage (faster operation), all of which can be attributed to vastly steep entropic energy barriers, which are enforced by larger entropy loss inside the capillaries due to 2D confinement (steric exclusion).

EXPERIMENTAL SECTION

Fabrication. The sieves were realized in a unique process described in ref 24 and illustrated in Figure S-1. The process began with standard 4 in. silicon wafers thermally oxidized to grow a 1 μm thick oxide layer and then sent to low-pressure chemical vapor deposition (LPCVD) to receive a 6 μm thick layer of low-temperature oxide (LTO). Standard UV lithography and advanced oxide etching (AOE) were applied, defining trenches 2 μm wide and deep into the LTO layer, followed by the deposition of a 100 nm thick low-stress nitride (LSN) layer as a diffusion barrier. LPCVD was applied to place a 5.5 μm thick layer of phosphorus-doped glass (phosphosilicate glass, PSG) allowing trenches to enclose due to the shadowing effect by the trench edges, forming self-enclosed conduits in triangular profile. For shape transformation into cylindrical capillaries, thermal reflow was performed by annealing the wafers at 1000 $^\circ\text{C}$ for 60 min. This was followed by chemical mechanical polishing (CMP) to ensure a planar surface while reducing the PSG layer thickness down to 2 μm . The steps of standard UV lithography and AOE were repeated to create the reservoirs for the sample and buffer as well as fluidic channels 2 μm wide and deep into the PSG and the underneath LTO layers. Sufficiently thick LTO layer was left behind to sustain a high-voltage separation. Rapid thermal annealing (RTA) was applied repeatedly to controllably shrink the capillary diameter down to either 70 nm for those sieves to fractionate through electrostatic interactions or 300 nm for those to fractionate through steric interactions. For the latter, the diameter was further scaled to 70 nm by the ALD of alumina. The sieves were bonded with a poly(dimethylsiloxane) (PDMS) cover featuring inlet/outlet ports through an oxygen plasma surface activation (29.6 W Harrick Plasma, 65 s).

Reagents. Double-stranded DNA (dsDNA) fragments of various sizes, including fragments with chain lengths in kbp of 5, 10, 20, and 48.5 (from bacteriophage λ cI857 Sam7, λ -DNA), along with the protein cholera toxin subunit B (11.4 kDa) conjugated with Alexa Fluor 488 and YOYO-1 intercalating dye, were all purchased from Thermo Fisher Scientific (Waltham, MA). The bacteriophage T4 GT7 DNA (166 kbp) was obtained from Nippon Gene (Tokyo, Japan). Green

fluorescent protein (GFP) was purified from GFP-over-expressing *Escherichia coli* through chromatography columns. Cytochrome *c* from equine heart, bovine serum albumin (BSA), tris, borate, fluorescein isothiocyanate (FITC), and dimethyl sulfoxide (DMSO) were purchased from Sigma Chemicals Co. (St. Louis, MO). Ethylenediaminetetraacetic acid (EDTA), sodium dodecyl sulfate (SDS), and dithiothreitol (DDT) were acquired from Sigma-Aldrich (St. Louis, MO).

All the dsDNA samples were dissolved in 5× TBE buffer (445 mM Tris/borate, 10 mM EDTA, pH ~ 8.3) at a concentration of 50 μg/mL after being labeled with YOYO-1 at a dye/base pair ratio of 1:10. The proteins, including BSA, GFP, and cytochrome *c*, were labeled with FITC and subsequently mixed with 2 wt % SDS and 0.1 mM DDT. The mixture was incubated in a water bath at 80 °C for 10 min. The SDS-denatured proteins were then further diluted with 5× TBE buffer with the resultant mixture containing 0.2 mg/mL denatured proteins, 0.1 wt % SDS, and 5 μM DTT.

Experiments. Each sieve was filled with the TBE buffer and placed on the stage of an epifluorescence microscope (Eclipse, Nikon, Tokyo, Japan) equipped with a 100 W mercury lamp and a filter cube set for the excitation and detection of fluorescent emissions (Ex/Em: 491/509 nm, YOYO-1; 488/525 nm, Alexa Fluor 488). Air bubbles were removed by running electroosmosis for a few hours.²⁹ The continuous streams of dye-labeled proteins and DNA molecules were generated and fractionated in the sieve under two independent and orthogonal direct-current electric field vectors delivered from a multichannel high-voltage power supply (Tianjin Dongwen Co. Ltd., Tianjin, China) through platinum electrodes (Leego Precision Alloy, Shanghai, China) immersed in the reservoirs. Electrical configuration is illustrated in Figure S-2. A thermoelectric-cooled electron-multiplying charge-coupled device (EMCCD) (iXon3897, Andor, Dublin, Ireland) was used to capture the stream images. Fluorescence intensity profiles from a select region were extracted and analyzed by an image processing software (ImageJ; NIH, Bethesda, MD). Essential parameters, including the mean, x_i , and standard deviation, σ_i , of a stream i , were derived from a Gaussian fit to the corresponding peak (OriginPro 8.5, OriginLab Corp., Northampton, MA). The separation resolution between any two streams (streams 1 and 2) was obtained through the relation $R_s = 2(x_1 - x_2)/(\sigma_1 + \sigma_2)$. The peak capacity of the sieve n_c was calculated according to $n_c = (L_c + 2\bar{\sigma}_m)/4\bar{\sigma}_m$, where L_c is the separation distance along the x -axis direction which was taken here as the distance between the two separated streams at the sieve end, $L_c = x_n - x_1$, with $x_n > x_1$, and $\bar{\sigma}_m$ is the mean of the stream standard deviations σ_1 and σ_n . The distance L_c was estimated as $L_c = l(\tan \theta_n - \tan \theta_1)$ where θ_n and θ_1 represent the stream deflection angles, with $\theta_n > \theta_1$, and l is the array length along the y -axis direction ($l = 5000 \mu\text{m}$).

RESULTS AND DISCUSSION

Sieve Structure. Figure 2 shows the scanning electron microscopy (SEM) images of various segments from a representative sieve. The sieve contains a 2D periodic CW array 5 mm wide and long, featuring self-enclosed capillaries that are 70 nm in diameter and 2 μm long, being separated by 2 μm wide and deep channels (pitch, 4 μm). Results from sieves featuring a pitch 10 and 20 μm are also presented (Supporting Information). As illustrated in Figure 2a (and in Figure S-2), the array is accessed by buffer reservoirs situated all around, through channels 2 μm wide and deep as well. Each channel

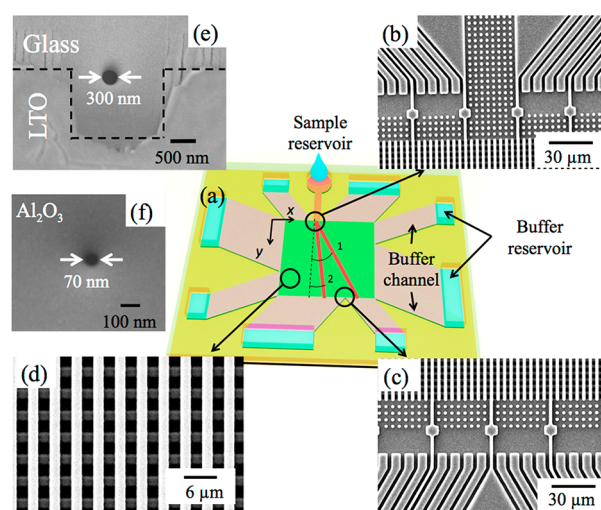


Figure 2. Scanning electron micrographs from a representative sieve captured from various sites as marked on (a) the layout schematic: (b) the sample injection channel, (c) the sample collection channels, (d) the sieve array, and the cross-sectional views of a single capillary (e) before and (f) after placing an Al_2O_3 layer. Pitch, 4 μm (capillaries, 2 μm long).

exerts a high electrical resistance, functioning as a current-injection source when an electric potential is applied through wire electrodes immersed in the reservoirs. The current-injection method has been implemented in previous 2D sieves because it offers tunable uniform electric fields E_x and E_y established over almost the entire array, addressing the issue of highly distorted fields associated with a fixed voltage boundary applied in the absence of such resistors.^{21,22} A theoretical consideration of this method for a post array is given in ref 30. The sample injection channel (Figure 2b) is 34 μm wide and features 2 μm oxide pillars to prevent the aggregation of macromolecules and facilitate their delivery into the array. Fractionated molecules are collected at the opposing end (Figure 2c) in distinct streams deflected from the y -axis direction at a characteristic angle θ based on their size (illustrated in Figure 2a). A segment of the array featuring a pitch of 4 μm is depicted from above in Figure 2d.

In Figure 2e, a single capillary of the array is shown in a cross-sectional profile featuring a diameter 300 nm being scaled down through thermal reflow, whereas in Figure 2f, the capillary is shown being further scaled to 70 nm through ALD of an alumina layer at a precise thickness. Dimensions below 100 nm can also be achieved solely through a thermal reflow by extending the annealing duration as previously demonstrated for the 1D CW array.²⁴ Nevertheless, this annealing process is often interrupted by frequent inspections of the diameter. Scaling the diameter through ALD is highly predictable and conveniently performed in a single run. ALD offers a precise thickness control and a highly conformal step coverage over high-aspect-ratio structures.³¹ Moreover, the alumina capillary walls exhibit a weak surface charge density at the running buffer pH, ~8.3, since the isoelectric point (pI) of alumina is reportedly around 8.0,³² and thus, the unwanted electroosmotic flows can be suppressed during steric sieving macromolecules. Electrostatic sieving, however, requires negatively charged capillary walls, and the corresponding results presented here are based on a 70 nm sieve achieved entirely through a thermal reflow.

Sieve Characteristics. We first investigated the sieve characteristics purely based on the steric interactions of macromolecules. Thus, the experimental results obtained are from a sieve filled with TBE 5× buffer (ionic strength ~ 130 mM)³³ under which net electric charge of the sieve surface is being screened (the Debye length $\lambda_D < 1$ nm $\ll d_c = 70$ nm). Moreover, the alumina capillary walls express a surface charge density that is negligible at the stated buffer pH, ~ 8.3 . Steric interactions are concerned with conformation (entropic trapping) or configuration (Ogston sieving) of molecules according to the molecular size (the radius of gyration R_g) in relation to the capillary diameter, R . In entropic trapping, $R_g \gtrsim R$, larger molecules are more likely to deform and form hernias, which can initiate the jump process across a capillary; hence, between two consecutive jumps, larger molecules travel a shorter mean distance along the channels and follow a stream trajectory featuring a larger deflection angle θ (measured with respect to the y -axis direction as illustrated in Figure 2a).

Figure 3a shows a sequence of fluorescent images captured from a location where the array meets the collection channels

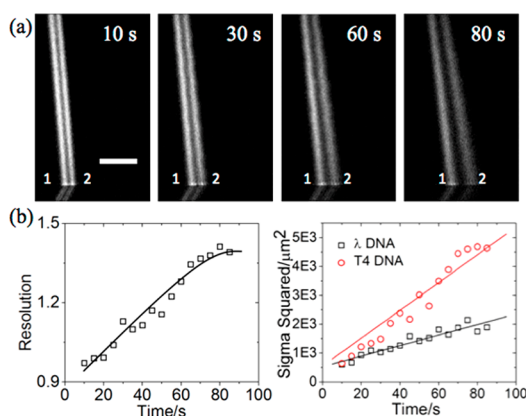


Figure 3. Continuous-flow electrophoresis of λ DNA and T4 DNA through a 70 nm CW array (pitch, 4 μm) under $E_x = 200$ V cm^{-1} and $E_y = 100$ V cm^{-1} . (a) Time-stamped fluorescent images captured near the collection channels. Stream assignments: (1) λ DNA and (2) T4 DNA. Scale: 400 μm . (b) Plots of the separation resolution R_s and the stream variance σ^2 over time.

(Figure 2c) during a continuous fractionation of bacteriophage λ DNA and T4 DNA. As can be seen, the two streams emerge ($R_s \sim 0.8$) in 10 s following the onset of the applied field strengths $E_x = 200$ V cm^{-1} and $E_y = 100$ V cm^{-1} . The spherical size of λ DNA (48.5 kbp) and T4 DNA (166 kbp) coils in equilibrium (unconfined), approximated by their radii of gyration ($R_g \sim 690$ and 1200 nm, respectively),³⁴ is greater than the sieve critical dimension ($d_c = 70$ nm). Crossing a capillary thus involves chain deformations and hernias nucleation (sieving by entropic trapping). A closer inspection at high magnification confirms that the migration of larger coils (T4 DNA) follows a more deflected stream trajectory than the migration of smaller coils (λ DNA).

In Figure 3b, the resolution, R_s , is shown to increase more or less linearly over time based on the fluorescence intensity profiles measured at the array bottom (Figure S-3). The streams are baseline-resolved within a minute following the field onset and over an area of 2 mm by 2 mm after leaving the injection point. More importantly, the streams are often fully resolved ($R_s \gtrsim 2$) with an increase in E_x up to around 600 V cm^{-1} , beyond which any further increase, however, rapidly

degrades the resolution due to the entropic energy barriers ran over by the intense field (Figure S-4). Figure 3b also shows the temporal profiles of the band dispersion (the variance of the Gaussian fits, σ^2). The bands gradually broaden over time for both the streams of λ DNA and T4 DNA. The latter disperses more severely than the former with a dispersion coefficient of 4.8×10^{-7} cm^2 s^{-1} ($R^2 \sim 0.93$) as opposed to 1.8×10^{-7} cm^2 s^{-1} ($R^2 \sim 0.96$).

For the entropic trapping regime, it is postulated that a large coil when pressed against a slit occupies a greater portion of the slit width and area than a small coil, which gives the large coil the opportunity of presenting more numbers of monomers to the slit than the small coil, thus rendering it statistically more prone to form hernias and subsequent jump escapes.¹⁹ This picture slightly differs here; a large DNA coil, whether be it T4 DNA or λ DNA, is sufficiently large to cover the entire capillary opening. Nevertheless, T4 DNA can be more densely packed against the capillary opening than λ DNA, with more numbers of monomers likely to initiate the escape. Since this increases the escape probability of T4 DNA coils as opposed to that of λ DNA, the stream of T4 DNA features a broader dispersion throughout the array (Figure 3b).

In the experiments, the field intensity applied, $E_x = 200$ V cm^{-1} , is the minimum requirement to launch the streams along the x -axis direction regardless of the molecular size of the species being separated. Such a distinct and intense field threshold for the band or stream launching is a distinguishing characteristic of the entropic barrier profiles arising from the capillaries and also observed in the 1D CW sieve,²⁴ yet at a much higher level (1000 V cm^{-1} ; the reason for the relatively low threshold is due to the structural geometry of the 2D CW sieve). Separation under intense fields is beneficial in terms of high speed and low dispersion. In comparison, however, the sieving mechanism in the SW sieve under such intense fields usually breaks down;¹⁹ typical field strengths applied in the 2D SW sieve remains around $E_x \lesssim 100$ V cm^{-1} .²²

The stream deflection angle θ is a direct measure of the size-dependent mobility of the macromolecules along the capillaries. The slope of the deflected stream can be approximated as

$$\tan \theta \sim \mu_x E_x / \mu_y E_y \quad (1)$$

where μ_y is the mobility inside the channels along the y -axis direction and taken here as the mobility in gel-free solution, $\mu_0 \sim 4 \times 10^{-4}$ cm^2 V^{-1} s^{-1} ,³⁵ and μ_x is the mobility along the x -axis direction. The mobility μ_x can be expressed in terms of $\mu_{x,\text{max}}$ which represents the maximum sieving-free mobility along the same direction, being treated here as a fitting parameter along with α_1 and α_2 :

$$\mu_x = \frac{\mu_{x,\text{max}}}{1 + \alpha_1 \exp(\alpha_2/E_x)} \quad (2)$$

Increasing E_x while keeping E_y constant at 100 V cm^{-1} (Figure 4a) increases the mobility of both λ DNA and T4 DNA chains along the capillaries in a trend nearly linear up to 600 V cm^{-1} and in excellent agreement with eq 1 (the fitting lines; $R^2 > 0.99$; α_1 and α_2 : $10.7\% \pm 1.8\%$ and 272 ± 38 V cm^{-1} , respectively, for λ DNA; $1.9\% \pm 0.7\%$ and 251 ± 23 V cm^{-1} for T4 DNA; $n = 5$). Notably, across the chains, the values of α_2 are comparable because the chains all encounter the same entropic barriers, whereas the values of α_1 vary by an order of magnitude, suggesting that T4 DNA spends a smaller fraction of the drift time along the x -axis direction inside the entropic

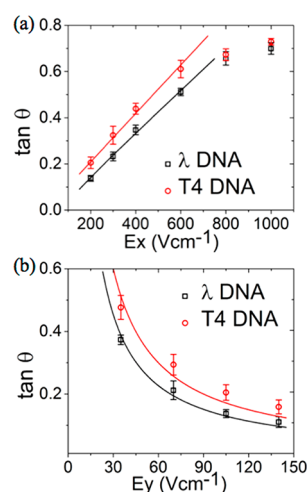


Figure 4. Plots of $\tan \theta$ as a function of (a) E_x , under E_y 100 V cm⁻¹, and (b) E_y , under $E_x = 200$ V cm⁻¹, obtained from continuous-flow electrophoresis of λ DNA and T4 DNA through a 70 nm CW array (pitch, 4 μ m). Error bars: ± 1 SD ($n = 5$).

traps than the fraction spent by λ DNA. Likewise, α_1 greatly varies with the pitch length (Figure S-5 and Table S-1) due to the reduced number of entropic traps; in 10 and 20 μ m pitch arrays, the value of α_1 for λ DNA drops to 2.4% \pm 0.3% and 0.1% \pm 0.01%, respectively, whereas $\mu_{x,\max}$ and α_2 show only a slight increase. Increasing E_x beyond 800 V cm⁻¹ causes the mobility values converged into $\mu_{x,\max}$ which corresponds to $\theta \sim 32^\circ$ and is consistent for the either chain size ($4.2 \pm 0.2 \times 10^{-5}$ cm² V⁻¹ s⁻¹ for λ DNA and $4.3 \pm 0.2 \times 10^{-5}$ cm² V⁻¹ s⁻¹ for T4 DNA). This value is an order of magnitude smaller than the conformation-independent free-draining mobility but larger than the value reported for λ DNA in 1D CW sieve (2.25×10^{-5} cm² V⁻¹ s⁻¹).²⁴

Increasing E_y , while holding E_x constant at 200 V cm⁻¹ (Figure 4b) leads to a reduced stream deflection angle because the chains migrate along the channels at an elevated rate while finding less and less time to explore the capillary crossings. Still, for a fixed E_y , T4 DNA exhibits a greater jump passage rate than λ DNA, resulting in a greater deflection angle θ . As E_y exceeds 100 V cm⁻¹, the discrepancy between the jump passage rates of λ DNA and T4 DNA chains diminishes. The trend exhibits a hyperbolic profile, which is in reasonable agreement with eq 1, and the values of $\mu_{x,\max}$ and the fitting parameters α_1 and α_2 are comparable to those obtained from Figure 4a ($4.2 \pm 0.1 \times 10^{-5}$ cm² V⁻¹ s⁻¹, 13% \pm 1.3%, and 267 \pm 25 V cm⁻¹ for λ DNA, $R^2 \sim 0.98$; $4.3 \pm 0.01 \times 10^{-5}$ cm² V⁻¹ s⁻¹, 3.1% \pm 0.6%, and 288 \pm 26 V cm⁻¹ for T4 DNA, $R^2 \sim 0.93$).

Sieving characteristics depend not only on the size of individual molecules being separated but also on the composition of the mixture these molecules are in. A mixture of DNA fragments featuring chain lengths of 10, 20, and 48.5 kbp is also shown successfully resolved into three distinct streams within a minute through a 4 μ m pitch sieve under the applied field strength $E_x \gtrsim 200$ V cm⁻¹ and $E_y = 100$ V cm⁻¹ (Figure 5a; movie in the Supporting Information). This separation still occurs in the entropic trapping regime where the jump dynamics of the DNA fragments are dictated by the chain deformation and hernia nucleation; the radii of gyration for all the fragments remain still well above the capillary diameter ($R_g \sim 320$ nm for 10 kbp DNA).³⁶ In Figure 5b, the deflections of all the three streams are shown to increase more

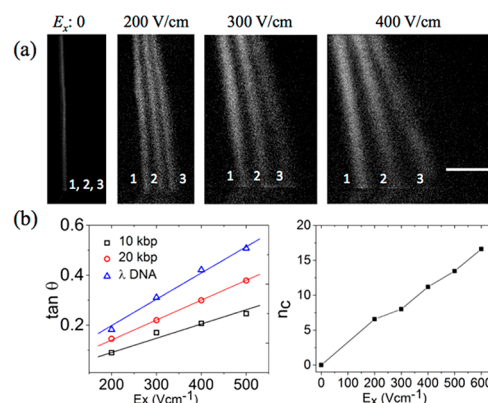


Figure 5. Continuous-flow electrophoresis of long DNA fragments through a 70 nm CW array (pitch, 4 μ m) under increased E_x and $E_y = 100$ V cm⁻¹. (a) Fluorescent images captured near the collection channels before and after the field onset along the x -axis direction with E_x being set to 200, 300, and 400 V cm⁻¹. Stream assignments in kbp: (1) 10, (2) 20, and (3) 48.5. Scale: 400 μ m. (b) Plots of $\tan \theta$ and the effective peak capacity n_c as a function of E_x .

or less linearly in response to an increase in E_x within the tested region ($E_x \lesssim 500$ V cm⁻¹ and $E_y = 100$ V cm⁻¹). As can be seen, the data are described reasonably well by the fitting lines according to eq 1 and for the values of $\mu_{x,\max}$, α_1 , and α_2 as listed in Table 1 ($R^2 \sim 0.99$ for 20 and 48.5 kbp DNA and $R^2 \sim 0.94$

Table 1. Fitting Parameters for the Plot of $\tan \theta$ Shown in Figure 5b

DNA length (kbp)	$\mu_{x,\max} \times 10^5$ (cm ² V ⁻¹ s ⁻¹)	α_1 (%)	α_2 (V cm ⁻¹)	R^2
10	4.02	75.9	95	0.944
20	4.00	26.2	96	0.999
48.5	4.45	7.4	120	0.992

for 10 kbp DNA). For λ DNA, while $\mu_{x,\max}$ is slightly larger than those obtained from the separation of λ DNA and T4 DNA (Figure 4), α_1 , and α_2 are considerably reduced in comparison. Although α_1 falls within the range of $\mp 2\sigma$ (see the fittings for Figure 4a), these discrepancies could originate from the structural variations across different devices as well as the variations due to molecular interactions specific to a particular composition of the mixture; T4 DNA (166 kbp) is a relatively large chain, and its presence could interfere with the jump dynamics of λ DNA as opposed to the presence of fragments 10 and 20 kbp.

A further measure of the separation efficiency is the maximum number of resolvable streams ($R_s \sim 1$) that can fit into the sieve, the so-called effective peak capacity of the sieve, n_c . Figure 5b additionally shows the dependence of the effective peak capacity n_c on E_x calculated in reference to the streams 10 kbp DNA and λ DNA. A constant increase in n_c is observed with an increase in E_x because of the enhanced lateral separation between the two streams. However, this trend is expected to level off at some point (when $E_x > 600$ V cm⁻¹) due to the increased dispersion of the streams with E_x . The peak capacity achieved here is comparable to that previously reported for the 2D SW sieve.²²

In Ogston sieving, where $R_g < R$, the stream of larger deflection angle constitutes smaller molecules as they are more likely to jump across a capillary than larger ones because larger molecules experience a relatively limited configuration freedom

inside a capillary and migrate a longer mean distance along the channels between consecutive jumps. Figure 6a shows an

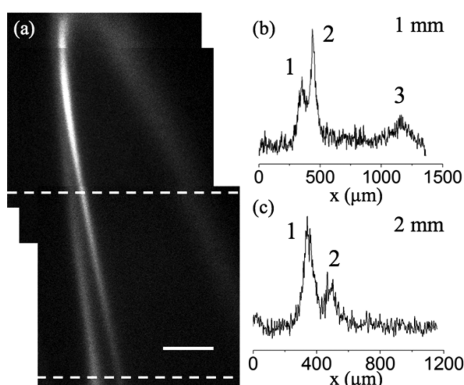


Figure 6. Continuous-flow electrophoresis of two SDS-denatured proteins through 70 nm CW array with 4 μm pitch under $E_x = 400 \text{ V cm}^{-1}$ and $E_y = 100 \text{ V cm}^{-1}$: (a) composite fluorescent image of the array below the injection point reconstructed from individual images captured after obtaining steady streams; (b and c) fluorescence intensity profiles obtained along the dashed lines located in panel a at (b) 1 mm and (c) 2 mm from the injection point. The peak assignments: (1) BSA ($\sim 68 \text{ kDa}$), (2) GFP ($\sim 27 \text{ kDa}$), and (3) free dye. Scale bar: 200 μm .

equimolar mixture of SDS-denatured BSA (68 kDa) and GFP (27 kDa), both in FITC-conjugated form, fractionated in a 70 nm sieve (pitch, 4 μm) filled with TBE 5 \times buffer under the field strengths $E_x = 400 \text{ V cm}^{-1}$ and $E_y = 100 \text{ V cm}^{-1}$. GFP complex, being smaller than BSA complex, migrates along the capillaries at a higher mobility, consistent with Ogston sieving, and following a trajectory deflected at a larger angle ($\theta \sim 14^\circ$ vs 8.5°). Parts b and c of Figure 6 show the fluorescence intensity plots along the x -axis direction at a distance of 1 and 2 mm from the injection point where the two streams are resolved with R_s values 0.8, and 1.1, respectively. The resolution at the sieve end ($R_s \sim 1.6$) can only be projected through a linear extrapolation of the Gaussian fits along the streams due to the weakened fluorescent signals. Moreover, the minimum resolvable size difference through the sieve is $R_M \sim 25 \text{ kDa}$ based on the differential size of the proteins forming the streams, ΔM , and the relation $R_M \sim \Delta M/R_s$. By comparison, the minimum resolvable size difference for the separation of denatured proteins in the 2D SW sieve is $R_M \gtrsim 70 \text{ kDa}$.²² It should be noted that a relatively low R_M value is achieved here using a pitch size twice as long, and thus, the number of entropic barriers twice as less.

Cholera toxin subunit B (11.4 kDa; $pI \sim 6.6$) and cytochrome c (12 kDa; $pI \sim 10$) are proteins of a comparable molecular size and thus cannot be separated at TBE 5 \times , in which electrostatic but steric interactions (Ogston) are excluded. Figure 7 (inset) proves that the separation of the two proteins leveraging steric interactions across the sieve is not viable. Nevertheless, the proteins exhibit pI values being sufficiently apart and suitable for a separation based on the native electrical charge at TBE 0.05 \times wherein electrostatic interactions are no longer screened (ionic strength, 1.3 mM; the Debye length $\lambda_D \sim 8.4 \text{ nm}$). At $pH \sim 11$, cytochrome c bears less negative charge than cholera toxin subunit B and thus will be repelled less by the capillary wall which features the same surface charge polarity. Because a sieve with an alumina surface coating ($pI \sim 8$) is charged weakly at the stated pH , and

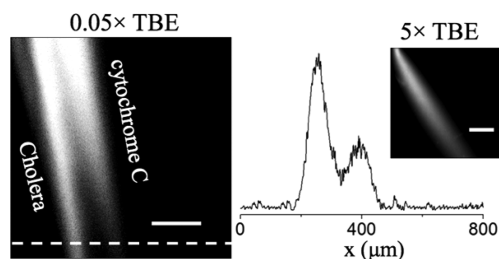


Figure 7. Continuous-flow electrophoresis of two native proteins through a 70 nm CW array (pitch, 4 μm) under $E_x = 200 \text{ V cm}^{-1}$ and $E_y = 100 \text{ V cm}^{-1}$. Fluorescent images captured below the sample injection point (scale bars, 200 μm): cytochrome c and cholera toxin shown being fractionated at TBE 0.05 \times but failing to fractionate at TBE 5 \times (inset). Fluorescence intensity profile along the dashed line. The scaling of the capillary diameter down to 70 nm was achieved entirely through a thermal reflow of doped glass to retain a negatively charged surface ($pH 11$).

cannot be that effective in electrostatic sieving, the sieve fabrication excludes the ALD of alumina and relies entirely on a thermal reflow to bring the capillary diameter down to 70 nm. Since the doped glass surface is negatively charged at the stated pH , cytochrome c shows more passage rate than cholera toxin subunit B and follows a stream trajectory deflected at a larger angle (17.5° vs 10.4°), whereas the latter molecules experience a greater repulsion from the capillary walls. This leads to the separation as shown in Figure 7. The resolution R_s values at 1.5 and 5 mm (extrapolated) from the injection point are 0.9 and 1.8 under field strengths $E_x = 200 \text{ V cm}^{-1}$ and $E_y = 100 \text{ V cm}^{-1}$, respectively. Moreover, the effective peak capacity $n_c \sim 4.6$ is comparable to that of the 2D SW sieve.²²

While we have found the continuous-flow sieving characteristics of the CW and SW sieves mostly comparable, the sieving of the SDS-denatured proteins is noticeably faster in the former (~ 68 and 27 kDa) than in the latter (~ 116 and 11 kDa ; Figure S2 in ref 22); the resolution level, $R_s \sim 1$, for instance, is attained at around 1 and 3 mm from the injection points, respectively. This feature directly arises from a relatively high-intensity field applied across the CW sieve along the x -axis direction, $E_x = 400 \text{ V cm}^{-1}$, in comparison to $E_x = 75 \text{ V cm}^{-1}$ applied for the SW sieve. Nevertheless, in the case of the SW sieve, the separation reaches maximum resolution at around $E_x = 100 \text{ V cm}^{-1}$, after which the resolution begins to degrade with a further increase in the field strength. The capacity to sustain the sieving mechanism under high-intensity fields is a unique characteristic of the CW sieve, which is also noticeable in batch operation and leads to a rapid separation.^{23,24} This feature arises from the 2D confinement inside the capillaries and correspondingly steep entropic barriers. Notably, the sieving characteristics that are otherwise comparable are obtained here through a CW sieve featuring a low-density entropic trap array (pitch, 4 μm) in relation to the reported SW sieve (pitch, 2 μm).²² The pitch was kept 4 μm instead of 2 μm , i.e., 2 μm long capillaries versus 1 μm long slits, to avoid expensive patterning tools (e.g., stepper); a typical contact aligner can reliably pattern features in size $\gtrsim 2 \mu\text{m}$.

A few remarks are in order regarding the size range of macromolecules that could be separated using the sieve. Ogston sieving of short DNA strands (length $\lesssim 1000 \text{ bp}$) may require even further smaller capillaries ($R \lesssim 50 \text{ nm}$), which is still within the realm of the fabrication method. Separation of megabase pair to chromosomal DNA chains requires larger

channels (wells) to allow sufficient relaxation of molecules ($R_g \gtrsim 3 \mu\text{m}$). This would, however, limit the packing density of entropic traps across the sieve and thus limit the effective separation of large DNA chains using a reasonably sized array. Probably, real limitation to effective separation of large DNA chains would come from strong electric fields applied to overcome steep entropic barriers and the inclination of large DNA chains to entangle and compress under such strong fields.³⁴ Indeed, we observed DNA aggregates gradually forming deposits along channels, causing the sieve performance to degrade over time. This limits the sieve runtime to less than an hour, and future remedies are needed should the sieve be used for a very large DNA or a longer duration.

CONCLUSION

We have demonstrated a 2D capillary-well array with a sieve size 70 nm and a pitch 4 μm and presented the sieve characteristics on the continuous-flow electrophoresis of small (proteins) as well as large (DNA) macromolecules. The sieve performance is found comparable, and even superior in the case of proteins, to that of the 2D slit-well array featuring a sieve size 55 nm and a pitch 2 μm . These results suggest that the steepness of the energy barriers across an entropic sieve array plays a crucial role on the separation performance and can be further enhanced by switching from slits (1D confinement) to capillaries (2D confinement). This alteration is observed highly effective in raising the energy barriers; comparable sieving results can be achieved by using nearly half of the entropic traps that would be otherwise needed. This relaxes the requirement on the spatial resolution of the array so that low-resolution patterning tools can be used without the concern over compromising the sieve performance. Conversely, advanced patterning tools can be applied for a high-resolution sieve (pitch $\lesssim 2 \mu\text{m}$) and, subsequently, enhanced separation quality, which would receive further boost from the use of capillaries.

ASSOCIATED CONTENT

Supporting Information

The Supporting Information is available free of charge on the ACS Publications website at DOI: 10.1021/acs.analchem.7b02484.

Supplementary figures and table regarding sieve layout and fabrication and further plots from sieving experiments (PDF)

Supplementary movie regarding long DNA fractionation in the sieve (AVI)

AUTHOR INFORMATION

Corresponding Author

*Phone: +852-2358 7068. Fax: +852-2358 1485. E-mail: eelyobas@ust.hk.

ORCID

Levent Yobas: 0000-0003-3151-5616

Notes

The authors declare no competing financial interest.

ACKNOWLEDGMENTS

This project was financially supported by the Research Grant Council of Hong Kong under Grants 621513 and 16203515.

REFERENCES

- (1) Matt, P.; Fu, Z. M.; Fu, Q.; Van Eyk, J. E. *Physiol. Genomics* **2008**, *33*, 12–17.
- (2) Ng, E.; Chen, K. N.; Hang, A.; Syed, A.; Zhang, J. X. *J. Ann. Biomed. Eng.* **2016**, *44*, 847–862.
- (3) Viovy, J. L. *Rev. Mod. Phys.* **2000**, *72*, 813–872.
- (4) Schwartz, D. C.; Cantor, C. R. *Cell* **1984**, *37*, 67–75.
- (5) Carle, G. F.; Frank, M.; Olson, M. V. *Science* **1986**, *232*, 65–68.
- (6) Slater, G. W.; Mayer, P.; Drouin, G. *Methods Enzymol.* **1996**, *270*, 272–295.
- (7) Volkmuth, W. D.; Austin, R. H. *Nature* **1992**, *358*, 600–602.
- (8) Han, J.; Craighead, H. G. *Science* **2000**, *288*, 1026–1029.
- (9) Baba, M.; Sano, T.; Iguchi, N.; Iida, K.; Sakamoto, T.; Kawaura, H. *Appl. Phys. Lett.* **2003**, *83*, 1468–1470.
- (10) Zeng, Y.; Harrison, D. J. *Anal. Chem.* **2007**, *79*, 2289–2295.
- (11) Dorfman, K. D. *Rev. Mod. Phys.* **2010**, *82*, 2903–2947.
- (12) Li, W. L.; Tegenfeldt, J. O.; Chen, L.; Austin, R. H.; Chou, S. Y.; Kohl, P. A.; Krotine, J.; Sturm, J. C. *Nanotechnology* **2003**, *14*, 578–583.
- (13) Cao, H.; Yu, Z. N.; Wang, J.; Tegenfeldt, J. O.; Austin, R. H.; Chen, E.; Wu, W.; Chou, S. Y. *Appl. Phys. Lett.* **2002**, *81*, 174–176.
- (14) Chou, C. F.; Bakajin, O.; Turner, S. W. P.; Duke, T. A. J.; Chan, S. S.; Cox, E. C.; Craighead, H. G.; Austin, R. H. *Proc. Natl. Acad. Sci. U. S. A.* **1999**, *96*, 13762–13765.
- (15) Rahong, S.; Yasui, T.; Yanagida, T.; Nagashima, K.; Kanai, M.; Klamchuen, A.; Meng, G.; He, Y.; Zhuge, F.; Kaji, N.; Kawai, T.; Baba, Y. *Sci. Rep.* **2015**, *4*, S252.
- (16) Zeng, Y.; He, M.; Harrison, D. J. *Angew. Chem., Int. Ed.* **2008**, *47*, 6388–6391.
- (17) van Oudenaarden, A.; Boxer, S. G. *Science* **1999**, *285*, 1046–1048.
- (18) Huang, L. R.; Cox, E. C.; Austin, R. H.; Sturm, J. C. *Science* **2004**, *304*, 987–990.
- (19) Han, J.; Turner, S. W.; Craighead, H. G. *Phys. Rev. Lett.* **1999**, *83*, 1688–1691.
- (20) Bakajin, O.; Duke, T. A. J.; Tegenfeldt, J.; Chou, C. F.; Chan, S. S.; Austin, R. H.; Cox, E. C. *Anal. Chem.* **2001**, *73*, 6053–6056.
- (21) Huang, L. R.; Tegenfeldt, J. O.; Kraeft, J. J.; Sturm, J. C.; Austin, R. H.; Cox, E. C. *Nat. Biotechnol.* **2002**, *20*, 1048–1051.
- (22) Fu, J. P.; Schoch, R. B.; Stevens, A. L.; Tannenbaum, S. R.; Han, J. Y. *Nat. Nanotechnol.* **2007**, *2*, 121–128.
- (23) Cao, Z.; Yobas, L. *Anal. Chem.* **2014**, *86*, 737–743.
- (24) Cao, Z.; Yobas, L. *ACS Nano* **2015**, *9*, 427–435.
- (25) Giddings, J. C.; Kucera, E.; Russell, C. P.; Myers, M. N. *J. Phys. Chem.* **1968**, *72*, 4397–4408.
- (26) Fu, J. P.; Yoo, J.; Han, J. Y. *Phys. Rev. Lett.* **2006**, *97*, 018103.
- (27) Liu, Y. F.; Yobas, L. *Biomicrofluidics* **2012**, *6*, 046502.
- (28) Duan, L.; Cao, Z.; Yobas, L. *Anal. Chem.* **2016**, *88*, 11601–11608.
- (29) Fu, J. P.; Mao, P.; Han, J. Y. *Nat. Protoc.* **2009**, *4*, 1681.
- (30) Huang, L. R.; Tegenfeldt, J. O.; Kraeft, J. J.; Sturm, J. C.; Austin, R. H.; Cox, E. C. Generation of large-area tunable uniform electric fields in microfluidic arrays for rapid DNA separation. In *Electron Devices Meeting, 2001. IEDM Technical Digest. International*, Washington, DC, Dec 2–5, 2001; IEEE: Piscataway, NJ, 2001; pp 363–366; DOI 10.1109/EDM.2001.979512.
- (31) Elam, J. W.; Routkevitch, D.; Mardilovich, P. P.; George, S. M. *Chem. Mater.* **2003**, *15*, 3507–3517.
- (32) Franks, G. V.; Gan, Y. *J. Am. Ceram. Soc.* **2007**, *90*, 3373–3388.
- (33) Weast, R. C.; Astle, M. J.; Beyer, W. H., Eds. *CRC Handbook of Chemistry and Physics*; CRC Press: Boca Raton, FL, 1988; Vol. 69.
- (34) Tang, J.; Du, N.; Doyle, P. S. *Proc. Natl. Acad. Sci. U. S. A.* **2011**, *108*, 16153–16158.
- (35) Stellwagen, N. C.; Gelfi, C.; Righetti, P. G. *Biopolymers* **1997**, *42*, 687–703.
- (36) Smith, D. E.; Perkins, T. T.; Chu, S. *Macromolecules* **1996**, *29*, 1372–1373.